EFDA–JET–PR(13)64

T. Koskela, M. Romanelli, P. Belo, O. Asunta, S. Sipilä, M. O'Mullane,
L. Giacomelli, S. Conroy, P. Mantica, M. Valisa, C. Angioni, P. Drewelow,
T. Kurki-Suonio and JET EFDA contributors

Effect of Tungsten Off-Axis Accumulation on Neutral Beam Deposition in JET Rotating Plasmas

Effect of Tungsten Off-Axis Accumulation on Neutral Beam Deposition in JET Rotating Plasmas

T. Koskela[2], M. Romanelli[1], P. Belo[3], O. Asunta[2], S. Sipilä[2], M. O'Mullane[4], L. Giacomelli[1,5], S. Conroy[6], P. Mantica[8], M. Valisa[9], C. Angioni[7], P. Drewelow[7], T. Kurki-Suonio[2] and JET-EFDA contributors*

JET-EFDA, Culham Science Centre, OX14 3DB, Abingdon, UK

[1]EURATOM-CCFE Fusion Association, Culham Science Centre, OX14 3DB, Abingdon, OXON, UK
[2]Aalto University, School of Science, P.O.Box 14100, FIN-00076 Aalto, Finland
[3]IPFN Laboratorio Associado, IST,P-1049-001 Lisboa, Portugal
[4]Department of Physics, University of Strathclyde, 107 Rottenrow, Glasgow, G4 0NG, Scotland
[5]Department of Physics, Universita degli Studi di Milano-Bicocca, Milano, Italy
[6]Department of Physics and Astronomy, Uppsala University, Uppsala, Sweden
[7]Max-Planck-Institut für Plasmaphysik, D-85748 Garching, Germany
[8]Istituto di Fisica del Plasma, CNR/ENEA, Milano, Italy
[9]Consorzio RFX-CNR/ENEA, I-35127 Padova, Italy
** See annex of F. Romanelli et al, "Overview of JET Results", (24th IAEA Fusion Energy Conference, San Diego, USA (2012)).*

Preprint of Paper to be submitted for publication in
Plasma Physics and Controlled Fusion

ABSTRACT

Evidence for low field side accumulation of tungsten is often observed in bolometry and soft X-ray emissivities of highly rotating JET ITER-like wall (ILW) plasmas. Poloidal variation of the density of high-Z impurities, such as tungsten, in the core of NBI heated plasmas is expected from neoclassical theory due to charge displacement and parallel electric field generated by the centrifugal force. We calculate the poloidally asymmetric distribution of tungsten using fluid equations and a 1D transport simulation with the JETTO/SANCO code. Peaking of tungsten on the outboard side of the plasma is found and verified with soft X-ray and bolometry measurements. We then study the effect of a poloidally asymmetric tungsten distribution on the distribution of the NBI heat source by simulations with the Monte Carlo code ASCOT. The simulations show that the poloidally asymmetric tungsten profile redistributes the fast NBI ions radially through shifting their ionization profile and poloidally through enhanced pitch-angle scattering at high energy. The amplitude of the redistribution is in the order of 10% for the highest n_W/n_e ratios of $\sim 10^{-4}$ measured in recent JET H-mode plasmas. The modelling is in agreement with measurements by the vertical neutron camera that sees a broadening in the 2.5MeV neutron profile when tungsten peaks on the outboard side of the plasma.

1. INTRODUCTION

With the installation of the JET ITER-Like Wall (ILW), the composition of impurities in JET plasmas has changed from dominantly carbon (JET C-wall) to beryllium (Be) and tungsten (W). Hybrid plasma Pulse No:s with the ILW have featured lower pedestal pressure but a higher electron temperature peaking [1, 2] than similar C-wall experiments. It is important to understand the differences in core heat transport that may have been brought about by the different plasma composition, which we also expect to find in ITER. To determine the heat transport in the core, we have to calculate the distribution of heat sources and sinks. The distribution of tungsten that determines the radiated heat sink, has been the topic of a number of recent studies [3, 4] (and references therein). However, the plasma composition could also play a part in the deposition of the NBI heat source by changing the fast ion distribution in the core plasma.

The centrifugal force from plasma rotation redistributes heavy impurities to the outboard side of the plasma [5]. When the flow velocity of a species becomes of the same order as its thermal velocity (Mach number of order one), centrifugal effects start to play an important role in the momentum balance equation [6]. This condition is easily achieved for heavy impurities, such as tungsten, in JET NBI-heated Pulse No's where the NBI power exceeds 15MW and the toroidal rotation velocities are of the order of 10^5 ms^{-1}. The centrifugal force along the magnetic field lines is balanced by the parallel pressure gradient and the parallel electric field, which translates to the poloidal asymmetry of the density of the impurity species. Bolometer and soft X-ray tomographies often observe this feature in the recent JET-ILW campaigns [7, 8, 9]. A similar behaviour had already been observed in dedicated nickel injection experiments in JET with the carbon wall [10, 11, 12] and in ASDEX [13]. In this paper we shall refer to the poloidal redistribution of tungsten due to the centrifugal

force simply as “tungsten redistribution”.

When neutral beam particles enter the plasma, they become ionized mostly through impact ionization and charge exchange reactions [14]. The average concentration of tungsten observed in JET-ILW plasmas is in the order of 10^{-4}–10^{-5} and does not have a significant effect on the beam particles. However, if the density profile of tungsten becomes peaked along the path of the beam, reaching a large local tungsten concentration (up to 0.1% of the electron density), we expect to see the beam ion source profile shift off-axis due to the larger cross-section of tungsten for beam ionization, shown in Figure 1. The change in the ionization profile of the beam, as well as scattering off heavy impurities has been predicted to influence the collisional heating profile of the core plasma as well as the neutron profile from beam-thermal fusion reactions [15]. The predicted change in the neutron rate provides a feasible way of verifying this prediction in JET Pulse No:s by measuring the neutron profile across the major radius.

In this paper we describe the modelling of neutral beam deposition in two JET- ILW H-mode Pulse No:s where the average tungsten concentration is in the order of 10^{-4} and significant off-axis peaking of tungsten has been observed. For simulating the beams we use the kinetic Monte Carlo code ASCOT [17, 18] that is integrated in the JET integrated modelling suite JINTRAC [19]. The ASCOT simulations require the 2D density profiles of tungsten, which are obtained by post-processing the flux surface averaged profiles calculated by the core impurity transport solver JETTO/SANCO in JINTRAC. In Section 2 we show how the 2D tungsten density profiles are extracted from flux surface averaged quantities calculated with JETTO/SANCO and compared to the available diagnostics. In Section 3 we use the 2D tungsten density profiles in ASCOT to simulate the change in the neutral beam deposition and compare the predicted beam- target neutron rates to those measured by a neutron camera. Summary and conclusions are presented in Section 4.

2. JINTRAC MODELLING OF THE 2D DISTRIBUTION OF TUNGSTEN

In this section we describe the steps taken to obtain realistic 2D impurity density profiles, required as input for ASCOT, from JETTO/SANCO simulations. JETTO/SANCO treats the core plasma as 1D and solves flux surface averaged profiles. To include the centrifugal effect in the solution, the 1D impurity density profiles are mapped into 2D a posteriori, using postprocessors UTC and SXRPY. The 2D impurity profiles are compared with radiation profiles measured by Soft X-ray cameras and bolometers, and the transport of impurities is tuned iteratively until an agreement is reached. This method has been successfully used in Ref [3] to validate drift-kinetic and gyrokinetic impurity transport simulations. In order to find the correct impurity density for our ASCOT simulations, we scan over the impurity transport in the analysis.

In order to calculate the flux surface averaged density profiles of tungsten we run an interpretive JETTO/SANCO simulation using time-averaged experimental data from high resolution Thomson scattering (HRTS) for electron temperature and density and charge exchange (CX) spectroscopy for rotation and ion temperature. We assume steady-state and solve for the distributions of all ionization

states of beryllium and tungsten with the SANCO code [20]. Initial conditions are chosen so that the total core radiated power from bolometry and Zeff from visible spectroscopy are reproduced. The JETTO postprocessors UTC and SXRPY map the flux surface averaged density of a heavy trace impurity I into 2D using the result derived in Appendix A,

$$n_I(\psi, \theta) = \langle n_I(\psi, \theta) \rangle \frac{exp\left(\frac{m^* \Omega^2(\psi)}{2T_i(\psi)} R^2(\psi, \theta)\right)}{\left\langle exp\left(\frac{m^* \Omega^2(\psi)}{2T_i(\psi)} R^2(\psi, \theta)\right)\right\rangle}. \quad (1)$$

Here is a flux label, θ is the poloidal angle, $m^* = m_I - Zm_iT_e/(T_e + T_i)$ is an effective impurity mass, Z is the charge state of the impurity, Ω is the angular frequency of toroidal plasma rotation, assumed equal for all species, T_i and T_e are ion and electron temperatures, respectively, R is the major radius and hfi denotes the flux surface average of function ⟨f⟩. Equation (1) has a maximum at θ = 0, it conserves the flux surface averaged density and retains an up-down symmetry. The radial position of the maximum is a function of hnIi and the term $m^* \Omega^2R^2/T_i$, the square of the Mach number of a species with mass m. To make the comparison to soft X-rays, the total emissivity from all ion species in the plasma is then calculated. This is done using emissivity coefficients from the ADAS database [16], the density profile from Equation (1) and the 1D JETTO/SANCO profiles. The total emissivity $\in_I$ of impurity I is calculated using the coefficients for line radiation of the charge state k of impurity I, lIk , and bremsstrahlung of the charge state k of impurity I, l^I_k.

$$\begin{aligned} {}_I(\psi, \theta) = {} & n_e(\psi) \sum_{k=0}^{Z_I - 1} n_k^I(\psi, \theta) l_k^I(n_e(\psi), T_e(\psi)) \\ & + n_e(\psi) \sum_{k=1}^{Z_I} n_k^I(\psi, \theta) r_{k-1}^I(n_e(\psi), T_e(\psi)), \end{aligned} \quad (2)$$

where n_e is the electron density, n^I_k is the density of charge state k of impurity I, and Z_I is the atomic number of impurity I. Note that the electron density and temperature are assumed 1D functions of ψ, but the impurity density is a 2D function of ψ and θ. Synthetic camera signals can be calculated from the total map of emissivity by straightforward line integration.

The JETTO/SANCO/UTC/SXRPY analysis was performed on a time slice of JET hybrid Pulse No: 82722 at 5.9s in Ref [3] and the tungsten profile was found to peak on the low field side (LFS). The best match to diagnostics was obtained with a tungsten density profile that peaks at mid-radius and drops to zero on axis and at the separatrix. We use that tungsten density profile, reproduced in figure 5, as an input for the ASCOT beam simulations. However, there is a large uncertainty in the calculated tungsten density at the edge of the plasma. Diagnostic coverage of impurities at the outboard edge is poor in JET, since the soft X-ray cameras filter out emission from cold plasma regions and the bolometer only has a few lines of sight capable of resolving the radial radiation

profile. Therefore, tungsten at the pedestal top would be missed by the present JET diagnostics. Since the edge tungsten concentration could not be measured, the boundary of the theoretical model in the previous study was set at r/a = 0.85 [3] and the concentration at the separatrix was set arbitrarily to 0. Here, we wish to assess the effect of the edge tungsten concentration on the beams in the ASCOT simulation by treating it as a free parameter and performing a scan.

To scan the effect of the edge tungsten concentration on the beam deposition we have analyzed another similar time slice, from hybrid 2T, 1.5MA Pulse No: 82794. The early evolution of this Pulse No: is similar to that of Pulse No: 82722 [3], as illustrated by the time traces shown in Figure 2. We can identify a phase from roughly 5.2s to 6.2s where the soft X-ray radiation seen by an edge channel (t25) is higher than that of a central channel (t19), which indicates off-axis tungsten peaking. This phase also shows better confinement (d) than the rest of the discharges, where the soft X-ray radiation peaks on the core channel. From this early phase, we have selected a time slice at 5.3s for the analysis. The kinetic profiles for this time slice were obtained from HRTS data for electron temperature and density and CX data for rotation, assuming $T_i = T_e$ in the core, based on edge CX T_i data, due to the poor quality of the core CX data. The fitted ne and Te profiles, shown in Figure 3 are the averages over several inter-ELM measurements in the vicinity of 5.3s. Due to the poor quality of the CX data, the core rotation profile has been linearly extended from the edge to avoid numerical problems in the exponential term of Equation (1). As a result, the core rotation may have been underestimated. The sensitivity of the results with respect to core rotation will be revisited in Section 3.2.

The transport coefficients of tungsten in the JETTO/SANCO simulation were set to match the line-integrated soft X-ray signals in the core, and the transport coefficients at the edge were varied to consider the effect of the edge transport barrier (ETB) on the tungsten profile. We consider two cases in addition to the Pulse No: 82722 low edge tungsten concentration case. Pulse No: 82794 with intermediate edge tungsten concentration, and 82794 with a high tungsten concentration on top of the edge transport barrier. The tungsten profiles from these three cases are shown in Figure 5. Figure 6(a) illustrates the calculated soft X-ray emissivity after postprocessing for the centrifugal effect with SXRPY and the comparison to the line-integrated soft X-ray measurements is displayed in Figures 6(c) and (d). As expected, the measured soft X-ray signals can be matched equally well while scanning the tungsten concentration at the top of the pedestal. The propagation of the uncertainty in the measurement of electron temperature (12 %) and density (6 %) to the simulated emissivity has also been considered. We find that the sensitivity of the simulated Soft X-ray emissivity to the experimental errors in the input is in the range of 30 %, which leaves some freedom in the fitting. The relative error of the measured soft X-ray signals is less than 10 %.

3. ASCOT MODELLING OF THE IMPACT OF THE TUNGSTEN REDISTRIBUTION ON NEUTRAL BEAM DEPOSITION

We have re-analyzed the JETTO/SANCO simulations of Pulse No's 82722 and 82794 described in

the previous section by replacing the routinely used 1D code PENCIL [21] for the calculation of the neutral beam heating with the 3D Monte Carlo code ASCOT. In ASCOT, the radial impurity density profiles produced by JETTO/SANCO are mapped to 2D using equation (1). Effective ionization coefficients from the ADAS database [16] are used for calculating the beam ionization. Besides the redistribution of impurities, the effect of rotation on other physical processes, e.g., collisional pitch angle scattering or fusion reaction cross-sections, has not been taken into account in ASCOT. It has been seen in TRANSP analysis that plasma rotation can have a significant impact on e.g. the beam-target neutron rate [22]. However, in order to quantify the effect of the centrifugal force, we have separated it from other effects of rotation.

ASCOT follows the trajectories of NBI test ions from the grounded grid of the injector, through entry to the plasma, ionization, scattering and slowing down, until thermalization or loss from confinement [23]. Once the JETTO/SANCO simulation has reached steady-state, ASCOT is launched and the simulation is run until all the test particles have reached thermal energy or been lost to the vessel wall. The simulation is repeated with and without the 2D treatment of tungsten density, and changes in the fast ion density distribution are studied. The ASCOT simulations were carried out with 10^5 test particles using realistic beam energies and power fractions. With 105 test particles the Monte Carlo error in the calculated profiles is negligible and the main source of error in the simulations is the uncertainty in the measured temperature and density profiles that are used as input. The error can be roughly estimated by repeating the simulations at the upper and lower bounds of the profile measurements, which results in an error of 6% for the fast ion density and power deposition and 12% for the neutron rate.

The distribution of impurities plays a part in several processes modelled in ASCOT. First, the beam ionization is calculated with a Monte Carlo algorithm [?] that calculates the probability for ionization taking into account the local plasma composition. Second, the slowing down and pitch angle scattering are modelled by Monte Carlo operators that operate on each particle species in the local background plasma [24, 25]. Plasma heating and torque are calculated separately for each species based on the collision operators. Finally, beam-target fusion reaction rates depend on the local dilution of the main plasma ions by the impurities and on the redistribution of the fast ions.

3.1. SIMULATION OF JET PULSE NO:S

The ASCOT simulations show that the tungsten redistribution shifts the beam ionization profile off-axis towards the LFS, due to the local increase in ionization cross- section. The relative change in the beam ion source along the plasma midplane due to the tungsten redistribution is shown in Figures 7(c)-(d). The volume integrated beam ion source is reduced within the $\rho = 0.5$ surface by 2.5% in Pulse No: 82722 and by 4.5% in Pulse No: 82794. The difference is due to the difference in the edge tungsten concentration, shown in Figure 7(a)-(b). Since the predicted change in the ion birth profile in all simulation cases is smaller than the estimated error in the simulation, this effect may be regarded as negligible. In addition, a 2D redistribution of the beam ions occurs outside $\rho =$

0.5 during their slowing-down. Figure 8(b) shows the change in the beam ion distribution in Pulse No: 82722, displayed in Figure 8(a), due to the tungsten redistribution. It indicates a decrease in beam ion density on the LFS and an increase on the high field side (HFS) outside mid-radius. The same can also be observed in Figures 7(e)-(f). This is an orbit effect due to increased pitch angle scattering on tungsten, which flattens the initially peaked velocity space distribution of the beam ions. Figure 9(a) shows this in the velocity space distribution in Pulse No: 82722, in the region of real space outlined in red in Figure 9(b). Beam ions are born on trapped orbits, around $v_{||}/v = 0.4$, marked by white circles in Figure 9, and they remain trapped at high energy, where ion-electron collisios dominate. The velocity distribution becomes more isotropic towards low energy where pitch angle scattering due to ion-ion collisions with the main plasma ions become significant. Since the ion-ion collision frequency scales with Z^2, pitch-angle scattering is enhanced by the presence of tungsten. When the tungsten profile is concentrated on the LFS, an increase of de-trapped high energy beam ions is seen in the simulations. Figure 9(b) shows the change in the beam ion velocity space distribution brought on by the centrifugal effect. The density profile broadens in pitch, across the energy spectrum, due to the pitch-angle scattering of the beam ions on tungsten. This leads to a lower trapped fraction on beam ions and, therefore, an increase of ions on orbits circulating the HFS. The beam ion density on the HFS increases by 10% in both analyzed Pulse No:s, regardless of the edge tungsten concentration, which is clearly above the estimated level of uncertainty. In addition, this effect would be very hard to explain by the uncertainty in the 1D density and temperature profiles, due to its asymmetric nature.

The simulations also show a deficit of beam-target neutrons produced near the axis, shown in Figures 7(g)-(h), due to the redistribution of the beam ions by the tungsten. However, the beam-target reactions are dominated by high energy particles and, therefore, the in-out asymmetry due to scattering is less pronounced. The on- axis deficit is not entirely compensated by the increase off-axis, where the bulk ion density and temperature are lower. For these plasma parameters, the volume integrated neutron yield decreases only by 2% due to the tungsten redistribution. A 2% change is unlikely to be seen by the neutron yield monitor, in addition to being smaller than the uncertainties in the simulation. Therefore, the only feasible way to detect the in-out asymmetry is by measuring local changes in the neutron profile, especially on the HFS where an increase of more than 12 % is predicted by the simulations. A similar change is seen in the heating power deposited by the beams on the plasma electrons and ions in Figures 7(i)-(j).

3.2. SENSITIVITY STUDY

The sensitivity of the model to the terms and hnWi in equation (1) was investigated to find out the parameter space where the tungsten redistribution would have a significant effect on quantities derived from the fast ion distribution, such as the beam-target fusion yield and the heating profile. To make a simple comparison, we integrate the fast ion density and the collisional heating profile inside mid-radius ($\rho \leq 0.5$), where the ASCOT simulations indicated a flux-surface symmetric

deficit in the fast ion distribution. As a third comparable quantity, we use the total volume integrated DD neutron rate. We scan the tungsten concentration $c_W = n_W/n_e$ and the toroidal rotation velocity vtor from the values observed in the experiment, $c_W \approx 10^{-4}$ and $v_{tor} \approx 3\times10^5$ m/s up to 4 times their nominal value.

The increase in both Ω and n_W increases the amount of tungsten redistributed to the outer midplane, determined by Equation (1). It should be noted that reducing T_i would have a similar effect. It can be seen in Figure 10 that increasing either or nW will almost linearly increase the redistribution of the fast ions from the core to the edge, the increase being roughly twice as steep with as a function of n_W. Since the uncertainty in these quantities due to the uncertainty in the kinetic profiles is roughly 6% for the fast ion density and power deposition and 12% for the neutron yield, to achieve a significant change in these parameters, an unrealistically high volume averaged tungsten concentration of over 5×10^4 would be required. Increasing the rotation velocity up to 10^6 m/s does not yet produce a significant effect.

3.3. COMPARISON OF ASCOT RESULTS TO NEUTRON CAMERA MEASUREMENTS

2.5 MeV neutrons are a good proxy for diagnosing the fast ion distribution in JET deuterium plasmas, since beam-target reactions are the dominant DD fusion reaction. The in-out asymmetry of the DD reaction rate profile in the poloidal plane can be best viewed by the vertical KN3 neutron camera, with nine channels looking down on the plasma from the top of the machine [26] as illustrated by Figure 11. A DD reaction rate profile in (R, z) is calculated by ASCOT using parametrized fusion cross-sections [27]. A synthetic neutron camera signal, comparable to a normalized measured signal, is obtained by integrating the profile along the lines of sight of the detector channels, neglecting neutrons born outside the viewing cone that reach the camera via scattering.

The time resolution of the raw KN3 neutron camera data was 2 kHz, but for this comparison the signal was averaged over 30 ms around the simulated timeslices and corrected with geometric factors. The averaging time was chosen to be short enough to capture the effect of the off-axis tungsten peaking within one inter-ELM period. Figure 12 shows the comparison of the measurements to the synthetic signals calculated from ASCOT for the same time interval. Overall, the agreement is satisfactory, although the central vertical channels in Pulse No: 82722 see roughly 20% less neutrons than predicted by the ASCOT simulation. This may be due to a sawtooth crash slightly before 5.9s that is not accounted for in the simulation.

The predicted effect of the tungsten redistribution on the simulated neutron signals is a broadening of the vertical camera profile, since the neutron rate decreases on-axis and increases off-axis as was shown in Figure 7(e). The horizontal camera can't see the in-out asymmetry and is only used as a consistency check. Even the vertical camera sees the effect very weakly, since it is aimed at the center of the plasma, as illustrated in Figure 11, and does not cover the inboard side where the simulations predict the largest effect, recall Figure 8(b). To look for the broadening of the profile due to tungsten redistribution, the vertical neutron camera measurements were compared to measurements

taken at a later time in the Pulse No:s, where the off-axis peaking of tungsten is no longer observed. This is indicated by the soft X-ray measurements shown in Figure 13(a). Between the chosen time slices, the plasma temperature and the power input remain unchanged, which implies that changes to the neutron profile should be due to changes in the impurity profiles. To compare the two time windows, the neutron camera signals have been normalized by the total number of counts across all channels. The comparison between the normalized neutron camera signals during and after off-axis tungsten peaking are shown in Figure 13(b) by the solid lines and closed symbols. In both Pulse No:s, a broadening of the neutron profile is seen during the tungsten off-axis peaking phase. The ASCOT simulations predict a similar trend due to the tungsten redistribution, regardless of the edge tungsten concentration, as shown by the dashed lines and open symbols in Figure 13(b).

SUMMARY AND CONCLUSIONS

In this paper we have studied the impact of the tungsten redistribution due to the centrifugal effect on neutral beam deposition. An analytical mapping from flux surface averaged quantities to the poloidal distribution of the tungsten density in a rotating plasma has been derived. The model for the poloidal redistribution of tungsten has been implemented in the post-processing tools for JETTO/SANCO and in the fast-ion tracing code ASCOT. The post-processing tools allow the calculation of synthetic soft X-ray signals that can be directly compared to the measurements, while the ASCOT implementation was used to study the neutral beam heating profiles and neutron rate in rotating JET hybrid plasmas with a tungsten impurity concentration.

Good agreement was found between the simulated and measured soft X-ray emissivity profiles when the expression for the poloidal asymmetry is applied to the tungsten profiles calculated with JETTO/SANCO in JINTRAC. Neutral beam simulations with ASCOT show that a redistribution of tungsten to the LFS redistributes NBI ions in the core plasma. The beam ion source shifts off-axis and the fast ion density on the high field side increases due to scattering of trapped particles to passing orbits. In JET Pulse No's 82722 and 82794, with $c_W \approx 10^{-4}$ and $v_{tor} \approx 3\times10^5$ m/s, the off-axis shift of the ion source was found negligibly small, but an in-out redistribution of order 10% in the fast ion density outside mid-radius was predicted by the simulations. Beam-target neutron rates calculated from the ASCOT simulation were in agreement with neutron signals measured by the neutron cameras. The trend in the neutron signals predicted by the simulations was also observed in the experimental data at a later time in the Pulse No:, where the tungsten density profile was no longer peaked off-axis. The impact of the fast ion redistribution on the flux-surface averaged beam heating profile is less than 10 % for the plasma parameters analysed in this paper, which correspond to highest observed tungsten peaking in recent JET experiments. Sensitivity studies show that a significant change in core heating due to tungsten redistribution would require a global tungsten concentration of order 10^{-3} that would lead to a radiative collapse of the plasma. Thus it is not expected that this effect plays a role in JET H-mode plasmas with .

ACKNOWLEDGEMENTS

This work was supported by EURATOM and carried out within the framework of the European Fusion Development Agreement. The views and opinions expressed herein do not necessarily reflect those of the European Commission. The main author would like to thank Drs B. Alper, C. Giroud, J. Flanagan, T. Schlummer and V. Kiptily for their help in acquiring and understanding JET data.

REFERENCES

[1]. M.N.A. Beurskens, L. Frassinetti, C. Challis, C. Giroud, S. Saarelma, B. Alper, C. Angioni, P. Bilkova, C. Bourdelle, S. Brezinsek, P. Buratti, G. Calabro, T. Eich, J. Flanagan, E. Giovannozzi, M. Groth, J. Hobirk, E. Jorin, M.J. Leyland, P. Lomas, E. de la Luna, M. Kempenaars, G. Maddison, C. Maggi, P. Mantica, M. Maslov, G. Matthews, M.-L. Mayoral, R. Neu, I. Nunes, T. Osborne, F. Rimini, R. Scannell, E.R. Solano, P.B. Snyder, I. Voitsekhovitch, P. de Vries, and JET-EFDA Contributors. Global and pedestal confinement in JET with a Be/W metallic wall. Nuclear Fusion, **54**(4).043001, 2014.

[2]. C. Giroud, G.P. Maddison, S. Jachmich, F. Rimini, M.N.A. Beurskens, I. Balboa, S. Brezinsek, R. Coelho, J.W. Coenen, L. Frassinetti, E. Jorin, M. Oberkoer, M. Lehnen, Y. Liu, S. Marsen, K. McCormick, A. Meigs, R. Neu, B. Sieglin, G. van Rooij, G. Arnoflux, P. Belo, M. Brix, M. Clever, I. Coey, S. Devaflux, D. Douai, T. Eich, J. Flanagan, S. Grünhagen, A. Huber, M. Kempenaars, U. Kruezi, K. Lawson, P. Lomas, C. Lowry, I. Nunes, A. Sirinnelli, A.C.C. Sips, M. Stamp, S. Wiesen, and JET-EFDA contributors. Impact of nitrogen seeding on confinement and power load control of a high-triangularity JET ELMy H-mode plasma with a metal wall. Nuclear Fusion, **53**(11).113025, 2013.

[3]. C. Angioni, P. Mantica, T. Pütterich, M. Valisa, M. Baruzzo, E. Belli, P. Belo, M. Beurskens, F. J. Casson, C. Challis, L. Frassinetti, C. Giroud, N. Hawkes, T.C. Henderand J. Hobirk, T. Koskela, L. Lauro Taroni, M. Lehnen, J. Mlynar, M.L. Reinke, M. Romanelli, and JET EFDA contributors. Tungsten transport in JET H-mode plasmas in hybrid scenario, experimental observations and modelling. Accepted for publication in Nuclear Fusion, 2014.

[4]. T. Pütterich, R. Dux, M. Beurskens, V. Bobkov, S. Brezinsek, J. Bucalossi, J.W. Coenen, I. Coffey, A. Czarnecka, E. Joffrin, et al. Tungsten screening and impurity control in JET. In Proc. 24th IAEA Fusion Energy Conf.(FEC2012), San Diego, USA, pages 8{13, 2012.

[5]. F.L. Hinton and S.K. Wong. Neoclassical ion transport in rotating axisymmetric plasmas. Physics of Fluids (1958-1988), **28**(10).3082{3098, 1985.

[6]. M. Romanelli and M. Ottaviani. Effects of density asymmetries on heavy impurity transport in a rotating tokamak plasma. Plasma Physics and Controlled Fusion, **40**(10).1767, 1998.

[7]. P. Mantica, C. Angioni, M. Valisa, M. Baruzzo, P. Belo, M. Beurskens, C. Challis, E. Delabie, L. Frassinetti, C. Giroud, N. Hawkes, J. Hobirk, E. Joffrin, L. Lauro Taroni, M. Lehnen, J. Mlynar, T. Pütterich, M.Romanelli, and JET EFDA contributors. Transport analysis of tungsten and beryllium in JET hybrid plasmas with the ITER-like wall. In Proc. 40th EPS Conference

on Plasma Physics, Europhysics Conference Abstracts, page P4.141, Espoo, Finland, 2013.

[8]. P. Mantica, C. Angioni, F.J. Casson, T. Pütterich, M. Valisa, M. Baruzzo, P.C. da Silva Aresta Belo, I. Coffey, P. Drewelow, C. Giroud, N.C. Hawkes, T.C. Hender, T. Koskela, L.Lauro Taroni, E. Lerche, C.F. Maggi, J. Mlynar, M. O'Mullane, M.E. Puiatti, M.L. Reinke, M.Romanelli, and JET EFDA contributors. Understanding and Controlling Tungsten Accumulation in JET Plasmas with the ITER-like Wall. In Proc. 41th EPS Conference on Plasma Physics, Europhysics Conference Abstracts, page P1.011, Berlin, Germany, 2014.

[9]. T.C. Hender, B. Alper, C. Angioni, Y. Baranov, M. Baruzzo, P. Buratti, F.J. Casson, C.D. Challis, P. Mantica, C. Marchetto, M. Romanelli, S. Sharapov, and JET-EFDA contributors. Influence of MHD on impurity peaking in JET. In Proc. 41th EPS Conference on Plasma Physics, Europhysics Conference Abstracts, page P1.011, Berlin, Germany, 2014.

[10]. H. Chen, N.C. Hawkes, L.C. Ingesson, M. von Hellermann, K-D Zastrow, M.G. Haines, M. Romanelli, and N.J. Peacock. Poloidally asymmetric distribution of impurities in joint european torus plasmas. Physics of Plasmas, **7**.4567, 2000.

[11]. B. Alper, A.W. Edwards, R. Giannella, R.D. Gill, L.C. Ingesson, M. Romanelli, J. Wesson, and K. D. Zastrow. Strong asymmetries in impurity distributions of JET plasmas. In Proc. 23rd EPS Conference on Plasma Physics, Europhysics Conference Abstracts, Kiev, Ukraine, 1996.

[12]. L.C. Ingesson, B. Alper, H. Chen, A.W. Edwards, G.C. Fehmers, J.C. Füchs, R. Giannella, RD Gill, L. Lauro-Taroni, and M. Romanelli. Soft x ray tomography during elms and impurity injection in JET. Nuclear Fusion, **38** (11).1675, 1998.

[13]. P. Smeulders. Tomography of quasi-static deformations of constant-emission surfaces of high-beta plasmas in ASDEX. Nuclear Fusion, **26** (3).267, 1986.

[14]. S. Suzuki, T. Shirai, M. Nemoto, K. Tobita, H. Kubo, T. Sugie, A. Sakasai, and Y. Kusama. Attenuation of high-energy neutral hydrogen beams in high-density plasmas. Plasma Physics and Controlled Fusion, **40** (12).2097{2111, 1998.

[15]. T. Koskela, O. Asunta, P. Belo, M. O'Mullane, M. Romanelli, and S. Sipilä. Modelling of the effect of the iter-like wall on NBI heating in JET. In Proc. 40th EPS Conference on Plasma Physics, Europhysics Conference Abstracts, page P1.136, Espoo, Finland, 2013.

[16]. ADAS. Atomic data and analysis software. http.//www.adas.ac.uk/.

[17]. J. A. Heikkinen and S. K. Sipilä. Power transfer and current generation of fast ions with large-k_θ waves in tokamak plasmas. Physics of Plasmas, **2** (10).3724–3733, 1995.

[18]. E. Hirvijoki, O. Asunta, T. Koskela, T. Kurki-Suonio, J. Miettunen, S. Sipilä, A. Snicker, and S. Äkäslompolo. ASCOT. Solving the kinetic equation of minority particle species in tokamak plasmas. Computer Physics Communications, **185**(4).1310–1321, 2014.

[19]. M. Romanelli, G. Corrigan, V. Parail, S. Wiesen, R. Ambrosino, P. Belo, L. Garzotti, D. Harting, F. Köchl, T. Koskela, L. Lauro-Taroni, C. Marchetto, M. Mattei, E. Militello-Asp, M. Nave, S. Pamela, A. Salmi, P. Strand, G. Szepesi, and EDFA-JET Contributors. JINTRAC.

A System of Codes for Integrated Simulation of Tokamak Scenarios. Plasma and Fusion Research, **9**:34030231–34030234, 2014.

[20]. L Lauro-Taroni et al. Europhysics conference abstracts. In Proceedings of the 21st Conference on ,Controlled Fusion and Plasma Physics, Montpellier, volume 18, page 102, 1994.

[21]. C.D. Challis, J.G Cordey, H. Hamnen, P.M. Stubbereld, J.P. Christiansen, E. Lazzard, D.G. Muir, D. Stork, and E. Thompson. Non-inductively driven currents in jet. Nuclear Fusion, 29.563–570, 1989.

[22]. A. Pankin, D. McCune, R. Andre, G. Bateman, and A. Kritz. The tokamak Monte Carlo fast ion module NUBEAM in the national transport code collaboration library. Computer Physics Communications, **159** (3).157–184, 2004.

[23]. O. Asunta, J. Govenius, and T. Kurki-Suonio. Beamlet-based NBI-model for ASCOT. In Proceedings of the 13th European Fusion Theory Conference, page P1.01, 12–15. October 2009.

[24]. Allen H. Boozer and Gioietta Kuo-Petravic. Monte carlo evaluation of transport coefficients. Physics of Fluids, **24**(5).851–859, 1981.

[25]. E. Hirvijoki, A. Brizard, A. Snicker, and T. Kurki-Suonio. Monte carlo implementation of a guiding-center fokker-planck kinetic equation. Physics of Plasmas, **20** (9).092505, 2013.

[26]. L. Giacomelli, S. Conroy, G. Gorini, L. Horton, A. Murari, S. Popovichev, D. B. Syme, and JET EFDA Contributors. Tomographic analysis of neutron and gamma pulse shape distributions from liquid scintillation detectors at joint european torus. Review of Scientic Instruments, **85** (2):–, 2014.

[27]. H.-S. Bosch and G.M. Hale. Improved formulas for fusion cross-sections and thermal reactivities. Nuclear Fusion, **32** (4).611, 1992.

[28]. J.A. Wesson. Poloidal distribution of impurities in a rotating tokamak plasma. Nuclear Fusion, **37** (5).577, 1997.

Appendix A.

In this appendix we present the derivation of the equation of the 2D tungsten density distribution that is used in the postprocessing of JETTO. The intermediate result in Equation (A.7) is equal to the one obtained in [28], but this derivation is more general and valid for an arbitrary geometry. The final result in Equation (A.8) is a form that can be used directly in analyzing data from a 1D transport code such as JETTO.

We assume a trace impurity that has no effect on the equilibrium electric field. Equations will be written in plasma coordinates (ψ, θ, ϕ) which represent the poloidal magnetic flux and the poloidal and toroidal angles, respectively. For the laboratory frame, we will adopt cylindrical coordinates (R, ϕ, z), where R is the major radius and z is measured along the symmetry axis of the torus. The magnetic flux and the poloidal angle will be functions of the laboratory coordinates R and z and vice versa.

The equilibrium momentum equation of an impurity I with charge Z is [6]

$$-m_I n_I \Omega^2 R \hat{e}_R = -\nabla p_I + n_I Z e \left(\vec{E} + \vec{v_I} \times \vec{B} \right), \tag{A.1}$$

where m is the ion mass, n is the density, Z is the charge number, e is the unit charge, v is the velocity, $\vec{E}$ is the electric field and $\vec{B}$ is the magnetic field. The inertia term is the centrifugal force acting on the impurity species, Ω is the toroidal angular frequency (assumed to be the same for all ion species) and $\hat{e}_R$ is the unit vector in the direction of R.

Using toroidal symmetry, the unit vector in the direction of the magnetic field $\hat{b}$ can be expressed as

$$\hat{b} = \frac{B_\phi}{B} \hat{e}_\phi + \frac{B_\theta}{B} \hat{e}_\theta = \vec{b}_\phi + \vec{b}_\theta,$$

where $\hat{e}_\phi$ and $\hat{e}_\theta$ are the unit vectors in the toroidal and poloidal directions, respectively. The component of Equation (A.1) parallel to the magnetic field is

$$-m_I n_I \Omega^2 R \hat{e}_R \cdot \hat{b} = -\nabla p_I \cdot \hat{b} + n_I Z e \left(\vec{E} \cdot \hat{b} \right). \tag{A.2}$$

In the trace impurity approximation, the parallel electric field is generated by the plasma electron (e) and main ion (i) momentum balance

$$\begin{aligned} -m_i n_i \Omega^2 R \hat{e}_R \cdot \hat{b} &= -\nabla p_i \cdot \hat{b} + n_i e \left(\vec{E} \cdot \hat{b} \right), \\ 0 &= -\nabla p_e \cdot \hat{b} - n_e e \left(\vec{E} \cdot \hat{b} \right). \end{aligned}$$

Assuming quasineutrality $(n_e = n_i)$, and neglecting parallel temperature gradients we find

$$\vec{E} \cdot \hat{b} = -\frac{m_i \Omega^2 R T_e}{e \left(T_i + T_e \right)} \hat{e_R} \cdot \hat{b},$$

which substituted into Equation (A.2) gives

$$-m^* n_I \Omega^2 R \hat{e}_R \cdot \hat{b} = -\nabla p_I \cdot \hat{b}. \tag{A.3}$$

Here we have introduced the effective impurity mass $m^* = m_I - Z m_i T_e / (T_e + T_i)$, which is of the order of the impurity mass for $T_e \leq T_i$.

We note that, since $\hat{b} \cdot \hat{e}_\psi = 0$, both the pressure gradient and the radial unit vector in Equation (A.3) only contribute their poloidal component when projected in the direction of the magnetic field,

$$\begin{aligned} \hat{e}_R \cdot \hat{b} &= \hat{e}_R \cdot \vec{b}_\theta, \\ \nabla p \cdot \hat{b} &= \nabla p \cdot \vec{b}_\theta. \end{aligned} \tag{A.4}$$

We can write the impurity pressure gradient and its poloidal component as

$$\begin{aligned} \nabla p_I &= \frac{1}{\sqrt{g_{\psi\psi}}} \frac{\partial p_I}{\partial \psi} \hat{e}_\psi + \frac{T_i}{\sqrt{g_{\theta\theta}}} \frac{\partial n_I}{\partial \theta} \hat{e}_\theta, \\ \nabla p_I \cdot \vec{b}_\theta &= \frac{T_i}{\sqrt{g_{\theta\theta}}} \frac{\partial n_I}{\partial \theta} \frac{B_\theta}{B}, \end{aligned} \tag{A.5}$$

where the metric elements of the coordinate system are indicated by g. In particular

$$g_{\theta\theta} = \left(\frac{\partial R}{\partial \theta} \right)^2 + \left(\frac{\partial Z}{\partial \theta} \right)^2.$$

Here the impurity temperature is assumed to be equal to the main ion (e.g. deuterium) temperature. After inserting Equations (A.4) and (A.5), Equation (A.3) becomes

$$\frac{1}{n_I} \frac{\partial n_I}{\partial \theta} = \frac{m^* n_I \Omega^2 R}{T_i} \frac{B}{B_\theta} \sqrt{g_{\theta\theta}} \hat{e}_R \cdot \hat{b}.$$

It can be integrated between 0 and θ to give

$$n_I(\psi, \theta) = n_I(\psi, 0) \exp\left(\frac{m^* \Omega^2(\psi)}{T_i(\psi)} \int_0^\theta R(\psi, \theta) \frac{B}{B_\theta} \sqrt{g_{\theta\theta}} \hat{e}_R \cdot \hat{b} d\theta \right). \tag{A.6}$$

The integral in Equation (A.6) can be explicitly calculated for any flux function by noticing that $\sqrt{g_{\theta\theta}} d\theta = ds$, where s is the length of the magnetic field line projected on the poloidal cross section, and that for any function $f(R, z)$ and any curve γ in the (R, z) plane the relation $\nabla f \cdot t_\gamma = df/ds$ holds. Here t denotes the unit vector tangent to the curve γ. It follows that $\nabla R \cdot \hat{e}_\theta = \hat{e}_R \cdot \hat{e}_\theta = dR/ds$. Using the above relation we can write the integral as

$$\begin{aligned} &\int_0^\theta R(\psi, \theta) \frac{B}{B_\theta} \sqrt{g_{\theta\theta}} \hat{e}_R \cdot \hat{b} d\theta = \int_0^\theta R(s) \frac{dR}{ds} ds \\ &= \int_{R(\psi,0)}^{R(\psi,\theta)} R dR = \frac{1}{2} \left(R^2(\psi, \theta) - R^2(\psi, 0) \right), \end{aligned}$$

and, therefore, Equation (A.6) becomes

$$n_I(\psi, \theta) = n_I(\psi, 0) \exp\left[\frac{m^* \Omega^2(\psi)}{2 T_i(\psi)} \left(R^2(\psi, \theta) - R^2(\psi, 0) \right) \right]. \tag{A.7}$$

We note that the term in the exponent, $m^*\Omega^2 R^2/T_i$, is in fact the square of the Mach number of an ion species with the mass m^*. Equation (A.7) can be used to map the density profile $n_I(\psi, 0)$ measured on the midplane into a two-dimensional impurity distribution. One-dimensional transport codes such as JETTO, however, evolve flux surface averaged quantities and, therefore, we need to average Equation (A.7). The flux surface average $\langle f \rangle = \frac{1}{S}\int_\sigma f ds$ (where σ is a flux surface with the area S) of Equation (A.7) is

$$\langle n_I(\psi,\theta)\rangle = n_I(\psi,0)\left\langle \exp\left(\frac{m^*\Omega^2(\psi)}{2T_i(\psi)}R^2(\psi,\theta)\right)\right\rangle \exp\left(-\frac{m^*\Omega^2(\psi)}{2T_i(\psi)}R^2(\psi,0)\right).$$

To compare transport simulations with experimental results, it is therefore important to write the two-dimensional impurity density distribution in terms of the flux surface averaged density. In the limit of a low Mach number ($M \leq 1$) and large aspect ratio, the above average can be approximated as:

$$\langle n_I(\psi,\theta)\rangle \approx n_I(\psi,0)\exp\left(\frac{m^*\Omega^2(\psi)}{2T_i(\psi)}\left(\left\langle R^2(\psi,\theta)\right\rangle - R^2(\psi,0)\right)\right).$$

If the Mach number is significantly larger than one, as is often the case for heavy impurities in JET, the averaging has to be done for the entire exponential term and Equation (A.7), expressed as a function of flux surface averaged quantities only, becomes

$$n_I(\psi,\theta) = \langle n_I(\psi,\theta)\rangle \frac{\exp\left(\frac{m^*\Omega^2(\psi)}{2T_i(\psi)}R^2(\psi,\theta)\right)}{\left\langle \exp\left(\frac{m^*\Omega^2(\psi)}{2T_i(\psi)}R^2(\psi,\theta)\right)\right\rangle}. \tag{A.8}$$

The mapping $R(\psi,\theta)$ is usually only available numerically and therefore the averaging of the denominator has to be performed numerically as well. Equation (A.8) can be directly used to map the tungsten flux surface averaged profiles calculated with a 1D transport code, such as JETTO/SANCO, into a 2D distribution to be used in synthetic diagnostics and for postprocessing. This has been implemented in the UTC and SXRPY postprocessing tools in the JINTRAC suite of codes.

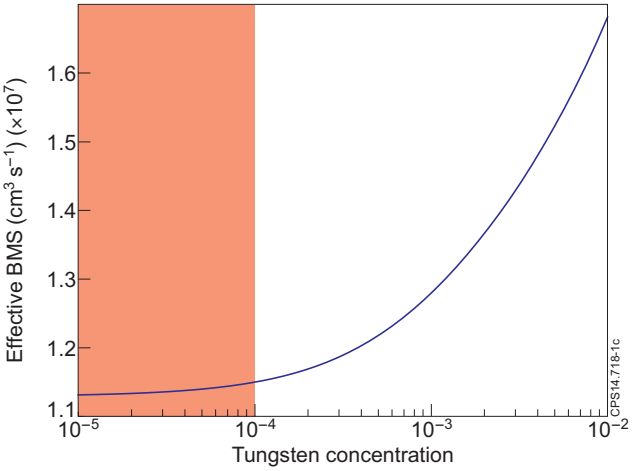

Figure 1: The eective beam stopping coefficient for a D plasma with a W impurity from the ADAS database [16]. The typical average tungsten concentration measured in JET plasmas is indicated by the shaded area.

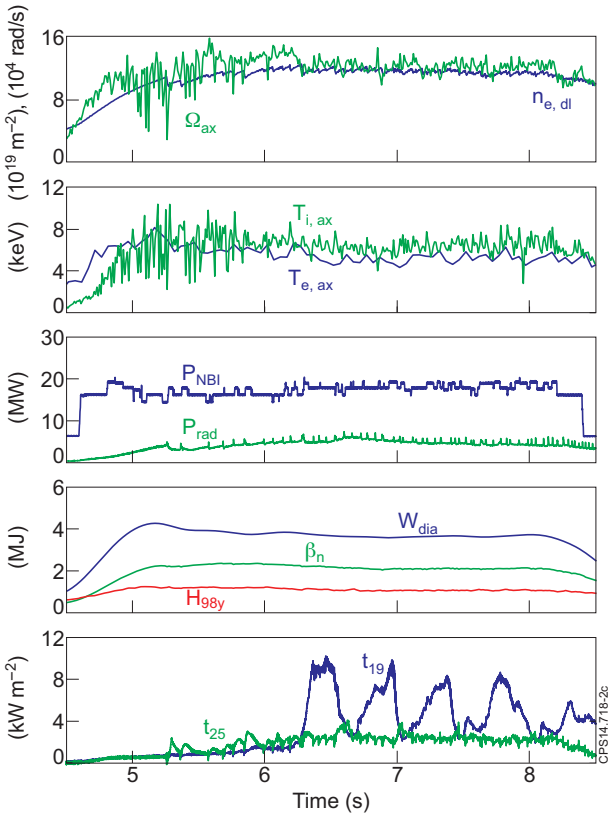

Figure 2: Time traces of JET Pulse No: 82794: (a) The line integrated density and central rotation, (b) central electron and ion temperature (c) NBI heating power and bulk radiated power (d) The stored energy W_{dia}, the normalized pressure β_n and the connement scaling factor H_{98y}, (e) line-integrated soft X-ray signal from a centrally viewing vertical channel (t19) and a peripherally viewing vertical channel (t25).

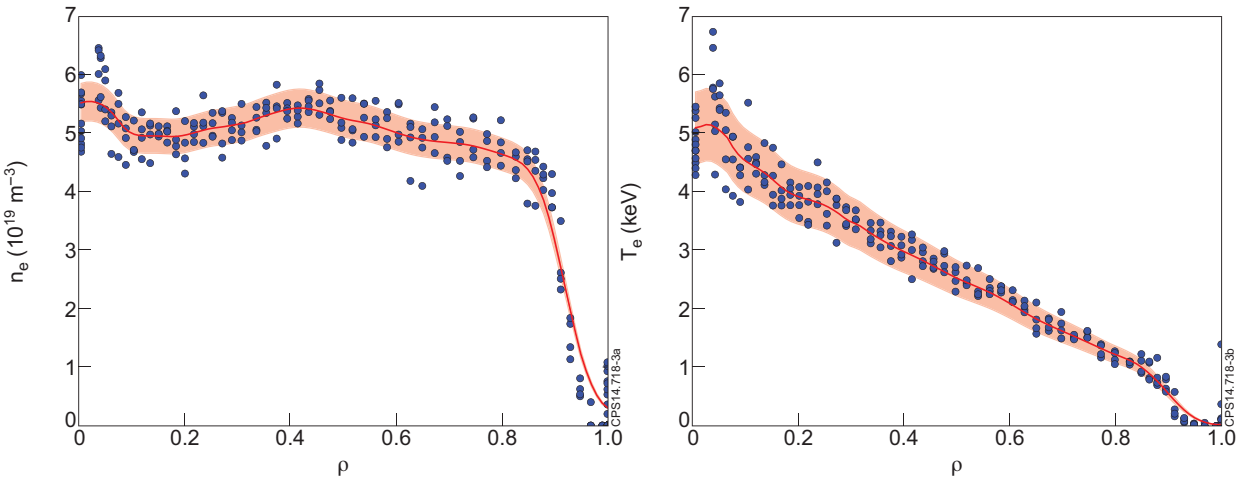

Figure 3: Kinetic 1D profiles for Pulse No: 82794 at 5.3s as a function of normalized toroidal flux. Electron density (a) and temperature (b): inter-ELM HRTS data points (blue points) time-averaged and smoothed (red line). The uncertainty in the data is indicated by the red shaded area.

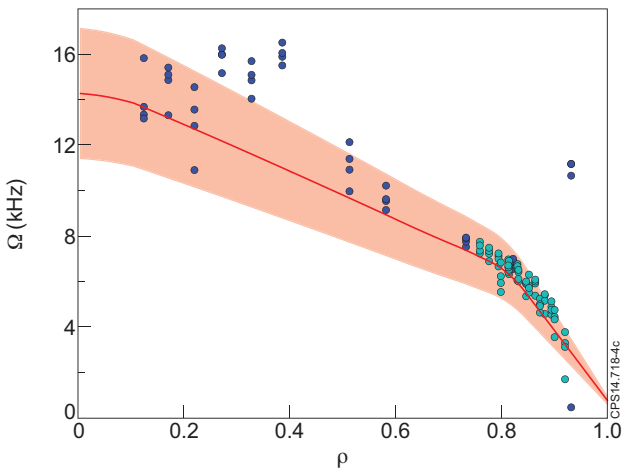

Figure 4: Toroidal rotation velocity measurements by core CX (blue points) and edge CX (cyan points). Due to the large scatter in the core data, the edge prole has been extrapolated linearly to the core (red line). This leaves a large uncertainty in the core profile, indicated by the red shaded region, that will be investigated in the sensitivity study in section 3.2.

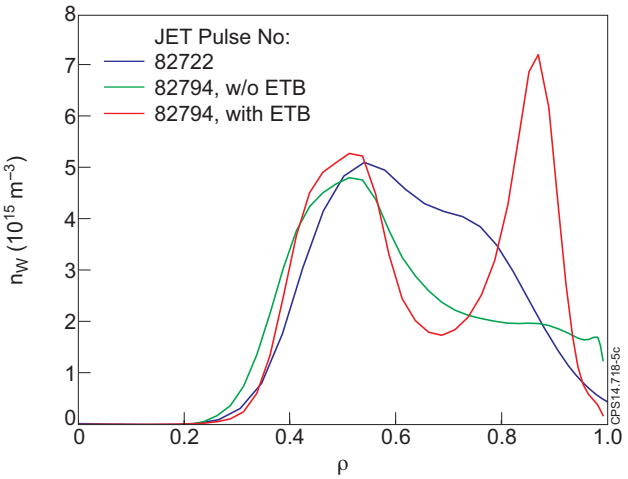

Figure 5: Flux-surface averaged tungsten density profiles calculated by JETTO/SANCO in the analyzed discharges. The tungsten concentration at ρ = 0.5 is kept approximately constant to match the soft X-ray signal, while the concentration outside ρ = 0.8 is scanned by changing the tungsten transport at the edge.

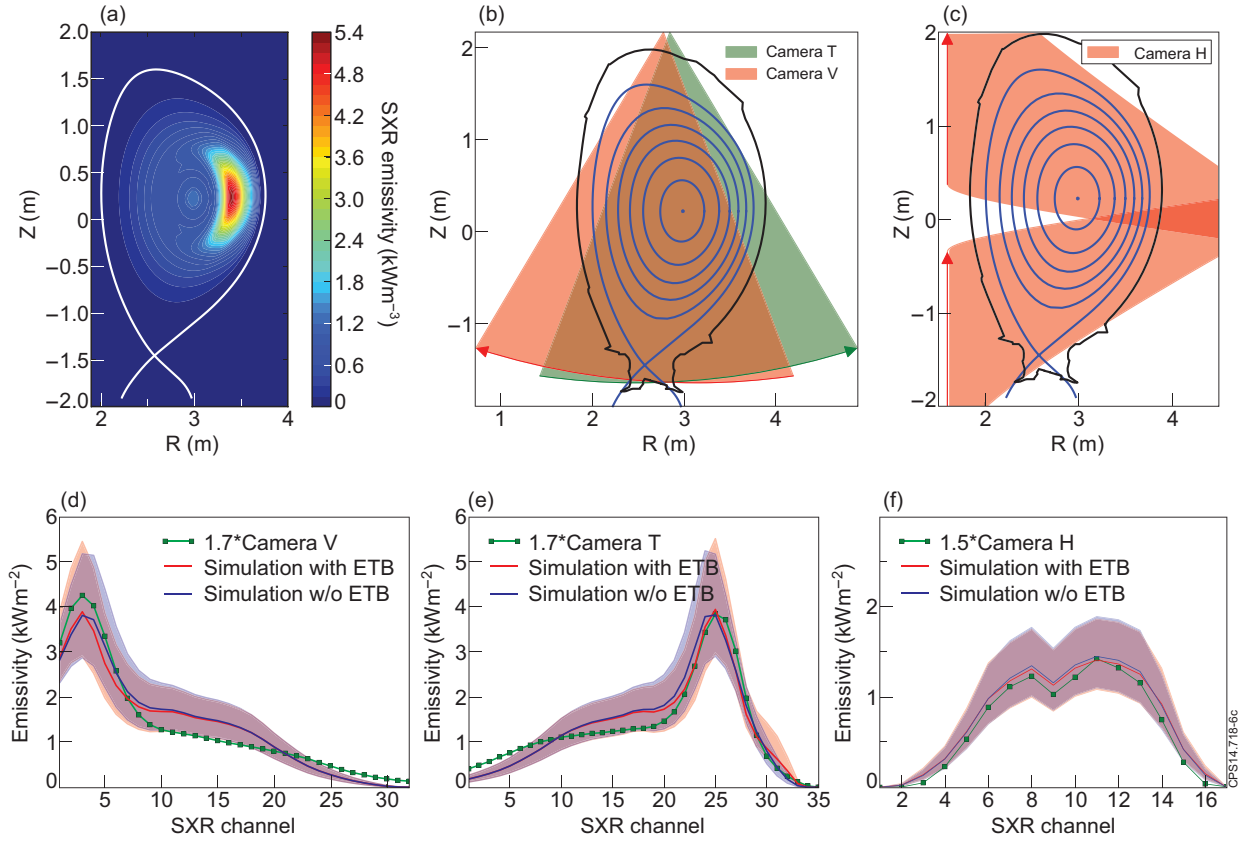

Figure 6: The simulated Soft X-ray emissivity in Pulse No: 82794 at 5.3s (a). The viewing cones of the vertical soft X-ray cameras are shown in (b) and the viewing cones of the horizontal camera are shown in (c), with the channel numbers increasing in the direction of the arrows. Simulated (solid lines) and measured (green rectangles) line-integrated Soft X-ray camera T (d), camera V (e) and camera H (f) signals, recalibrated by the factors found in Ref [3] are shown in the bottom panels. The shaded areas indicate the error bars of the simulated emissivities, due to the uncertainty in the temperature and density proles. The relative error of the measurement is less than 10%.

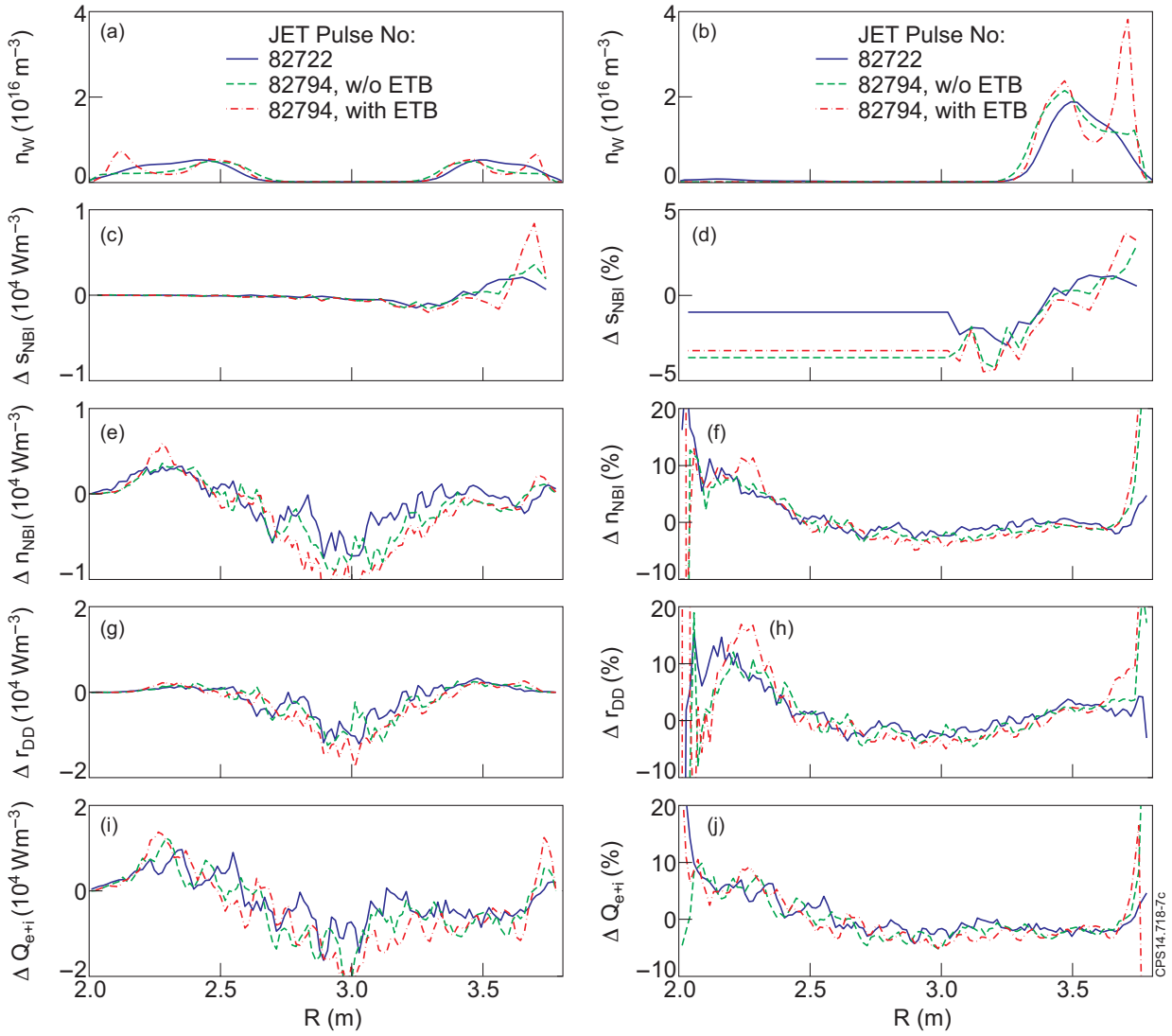

Figure 7: Tungsten density (nW) without the centrifugal effect (a) and with the centrifugal correction (b) along the midplane (z = zmag). The absolute (left column) and relative (right column) change due to the tungsten redistribution in fast ion derived quantities along the midplane (z = zmag): beam ion source (s_{NBI}) (c)-(d), beam ion density (n_{NBI}) (e)-(f), beam-target fusion rate (r_{DD}) (g)-(h) and the total heating power (Q_{i+e}) (i)-(j). Three simulations are shown, with different assumptions of tungsten transport at the edge, resulting in: low edge tungsten concentration (blue), medium edge tungsten concentration (green) and peaked edge tungsten concentration (red).

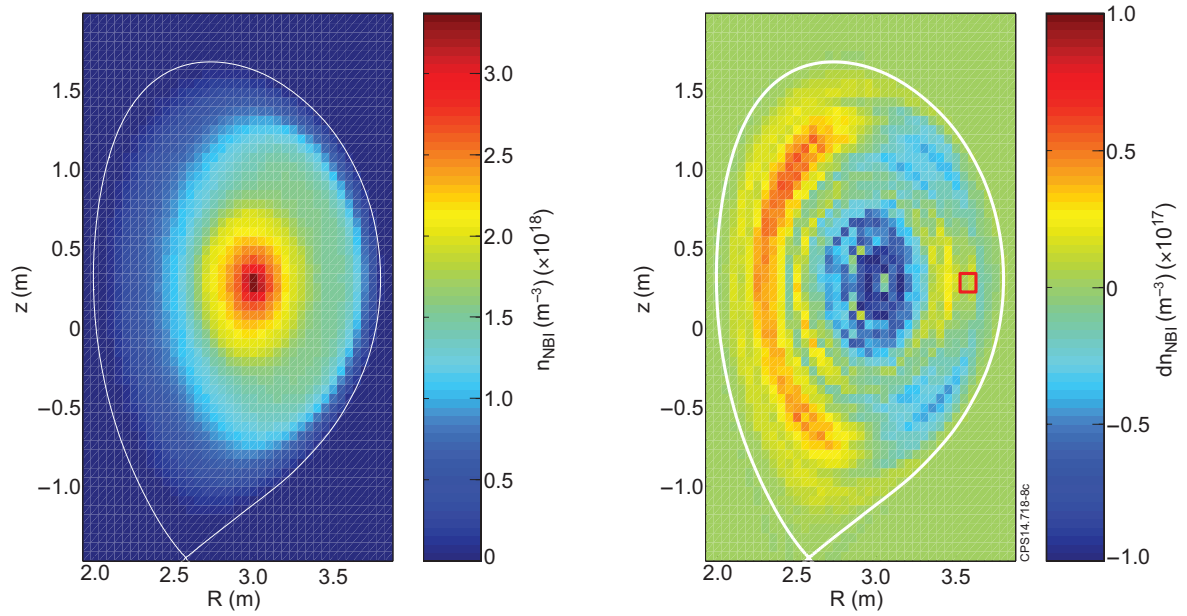

Figure 8: The simulated fast ion slowing-down density distribution in Pulse No: 82722 at 5.9s without the eect of tungsten redistribution (a). Panel (b) shows the simulated change in the fast ion distribution due to the tungsten redistribution.

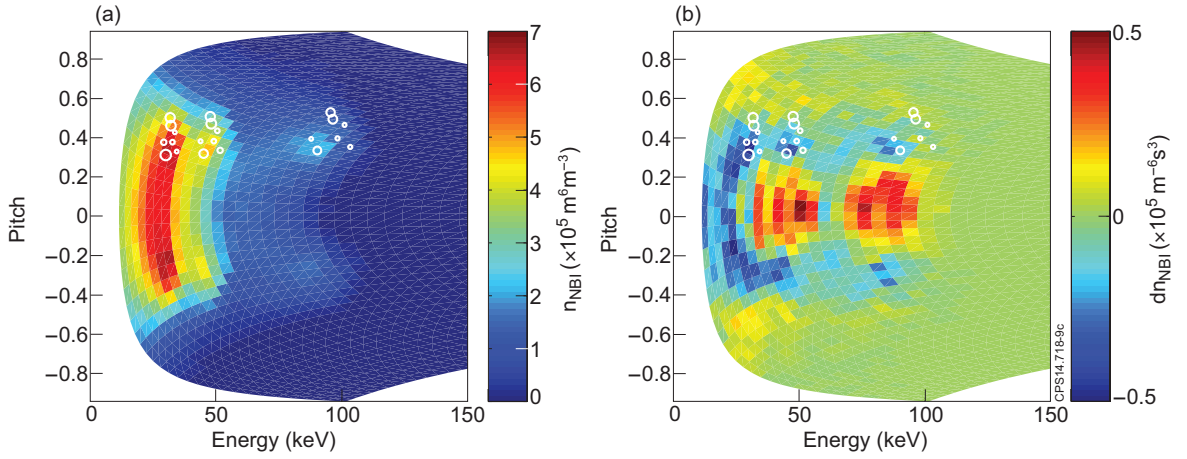

Figure 9: The NBI slowing-down density distribution in (pitch,energy) space in Pulse No: 82722 at 5.9s, averaged in real space over the peak of the tungsten distribution ($R \approx 3.5$m, $z \approx 0.3$m). Here pitch is the pitch angle cosine, $v_{||}/v$. Panel (a) shows the distribution without the eect of centrifugal force. The birth positions of the beam ions are indicated by white circles whose size represents the beam power. During slowing down, particles move down (to the left) in energy and scatter (up and down) in pitch. The change in the density (b) shows that pitch scattering increases when the centrifugal force is included. The distribution spreads to a wider range of pitch angles and the density close to the source decreases.

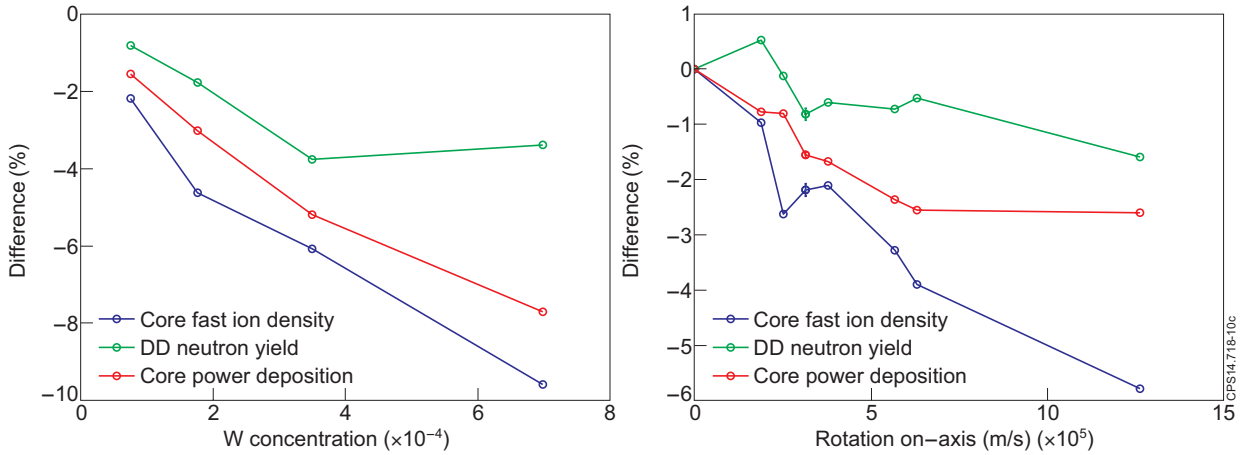

Figure 10: The sensitivitiy of 0-D quantities in the simulation of Pulse No: 82722 to volume averaged tungsten concentration (a) and rotation velocity (b). The y-axis shows the deficit caused by the tungsten redistribution. Here core stands for the region inside the ρ = 0.5 flux surface. The experimental values of vtor and c_W were $c_W \approx 10^{-4}$ and $v_{tor} \approx 3\times10^5$ m/s.

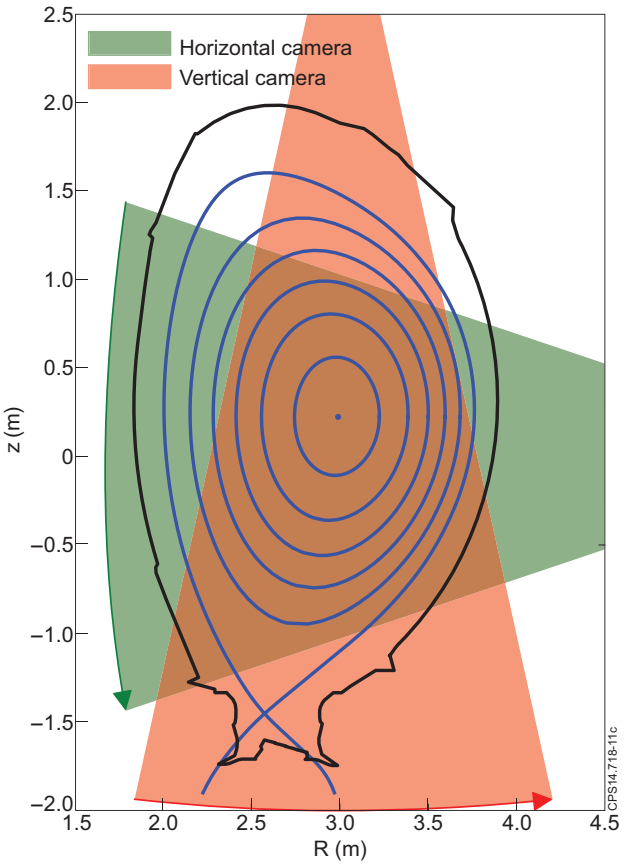

Figure 11: The viewing cones of the JET KN3 neutron camera. The channel numbers increase in the direction indicated by the arrows.

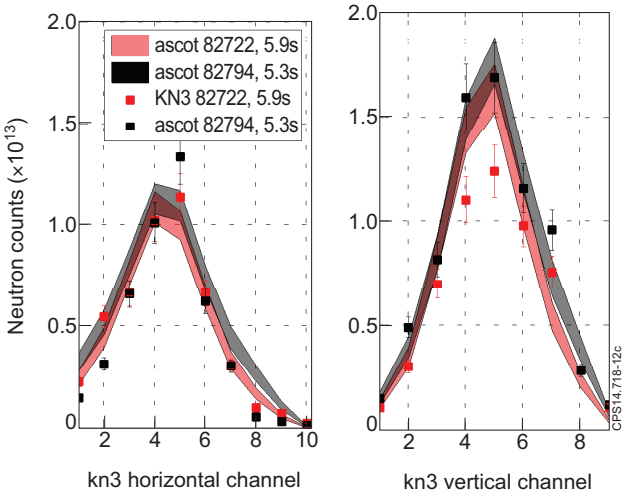

Figure 12: The signals measured by the KN3 neutron camera (squares) and the ASCOT simulated synthetic signals (shaded areas) the horizontal and the vertical neutron camera. The error in the measured signals is assumed to be 10%, the uncertainty in the simulated signals corresponds to the uncertainty in the plasma profile data.

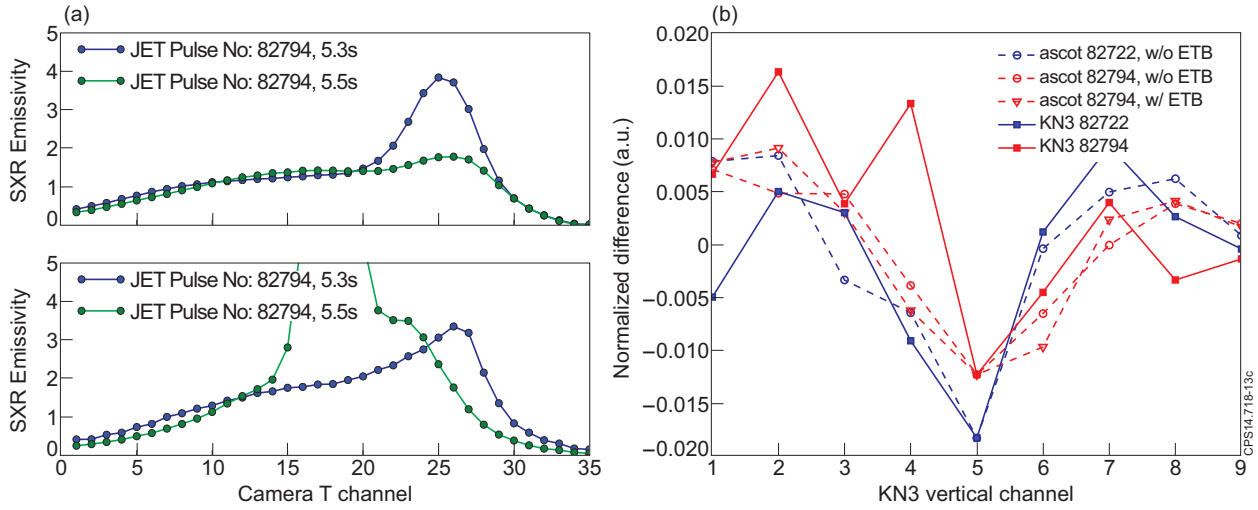

Figure 13: Soft X-ray measurements (a) at the selected time slices with and without off-axis tungsten peaking in Pulse Nos: 82722 and 82794. The dierence in normalized signals seen by the KN3 vertical camera (b) between 1) Pulse No: 82722 t = 5.9s and t = 7.5s (solid blue line), 2) Pulse No: 82794 t = 5.3s and t = 5.5s (solid red) 3) ASCOT simulations of Pulse No: 82722 t = 5.9s (dashed blue) and Pulse No: 82794 t = 5.3s (dashed red) with and without the tungsten redistribution. The simulations are normalized to match the measured dierence on channel 5.